RSC Advances

PAPER

View Article Online
View Journal | View Issue

Cite this: RSC Adv., 2014, 4, 53192

Synthesis and electrochemical performances of maricite-$NaMPO_4$ (M = Ni, Co, Mn) electrodes for hybrid supercapacitors†

Baskar Senthilkumar,[a] Kalimuthu Vijaya Sankar,[a] Leonid Vasylechko,[b] Yun-Sung Lee[c] and Ramakrishnan Kalai Selvan*[a]

Sodium metal phosphates, $NaMPO_4$ (M = Mn, Co and Ni) were successfully synthesized by a solution combustion synthesis (SCS) method using glycine-nitrate as a precursor. An XRD Rietveld refinement method revealed the crystal structure and lattice parameters of $NaMPO_4$ (M = Mn, Co and Ni). For the first time, the crystal structure parameters of the orthorhombic $NaNiPO_4$ maricite-type phase were evaluated. Similarly, it was identified that the $NaCoPO_4$ and $NaMnPO_4$ have high temperature hexagonal and maricite phases, respectively. The calculated BET specific surface areas (S_{BET}) of $NaMnPO_4$, $NaCoPO_4$ and $NaNiPO_4$ were 17.7, 22.6 and 18.7 $m^2\ g^{-1}$, respectively. The $NaMPO_4$ (M = Mn, Co and Ni) electrode exhibits good specific capacitance in 1 M NaOH electrolyte, when compared with 1 M Na_2SO_4, 1 M $NaNO_3$ and 1 M NaCl. This difference in specific capacitance was analysed based on the influence of electrolyte anions (Cl^-, SO_4^{2-}, OH^- and NO_3^-) and pH conditions of the electrolyte solution. Overall, maricite-$NaNiPO_4$ nanoparticles provided a high specific capacitance of 368 F g^{-1} compared to $NaMnPO_4$ (163 F g^{-1}) and $NaCoPO_4$ (249 F g^{-1}) in 1 M NaOH electrolyte. Subsequently, a hybrid supercapacitor (AC||$NaNiPO_4$) was fabricated and it delivered a good specific capacitance and cyclic stability compared to the commercially available device.

Received 21st June 2014
Accepted 6th October 2014

DOI: 10.1039/c4ra06050d

www.rsc.org/advances

1. Introduction

Among various energy storage devices, Li-ion batteries are promising power sources for cell phones, laptops, digital cameras, power tools and electric vehicles owing to their high energy density.[1,2] However their broad applications in grid storage are limited due to the high cost, low abundance of Li metal and organic electrolytes.[3] Next to Li, Na is second metallic element having lower ionic radius (0.97 Å) and similar intercalating properties of Li. Therefore in order to decrease the cost and improve the safety, using both Na-based intercalating materials and aqueous electrolyte used is one of the recent strategies instead of Li based materials.[3,4] In this regard, various sodium based electrode materials including $NaFePO_4$,[5] $Na_4Mn_9O_{18}$,[6] Na_xMnO_2,[7] $NaVPO_4F$,[8] $NaCrO_2$,[9] $NaNi_{1/3}Co_{1/3}Mn_{1/3}PO_4$,[10] $Na[Ni_{1/3}Co_{1/3}Mn_{1/3}]O_2$ (ref. 11) and $Na_4Co_3(PO_4)_2P_2O_7$ (ref. 12) have been experienced as electrode materials for energy storage applications due to its Na-ion intercalating properties, low cost and environmental friendliness.[5–12] Initially, layered sodium manganese oxide ($NaMnO_2$) has been proposed as cathode materials for Na-ion batteries.[7] Among the Na based cathodes, $NaMnO_2$ delivered high specific capacity of 140 mA h g^{-1} due to its six biphasic transitions.[13] However, these materials delivered poor cycling performance since its multiple phase transition during Na^+ insertion/de-insertion reactions.[7,14]

As well as sodium metal phosphates having the general chemical formula of $NaMPO_4$ (M = Mn, Co and Fe) have also been studied as electrode materials for sodium ion batteries.[5,15–17] Thermal stability and higher voltage due to the inductive effect are the reasons for phosphate based materials to be the promising cathode materials in Na-ion batteries.[18,19] Recently, $NaFePO_4$/C was prepared by potentiodynamic polarization in saturated aqueous $NaNO_3$ solution, which delivered a high storage capacity of 118 mA h g^{-1} compared to $LiFePO_4$/C.[20] Normally $NaMPO_4$ (M = Mn, Co and Fe) exhibits thermodynamically stable maricite structure, where transition metal ions occupies M(1) site, and sodium occupied M(2) sites, which is completely reversed in olivine structure. It was believed that the maricite structure is electrochemically inactive as a cathode material for battery applications in non aqueous media.[21] On the other hand, recent works demonstrated that the maricite structure is actively involved in charge storage process in alkali aqueous (NaOH) electrolyte.[10,15] However, to the best of our

[a]Solid State Ionics & Energy Devices Laboratory, Department of Physics, Bharathiar University, Coimbatore 641 046, India. E-mail: selvankram@buc.edu.in; Tel: +91-422-2428446

[b]Semiconductor Electronics Department, Lviv Polytechnic National University, 12 Bandera Street, Lviv 79013, Ukraine

[c]Faculty of Applied Chemical Engneering, Chonnam National University, Gwangju 500-757, Korea

† Electronic supplementary information (ESI) available. See DOI: 10.1039/c4ra06050d

knowledge, there is no report available on the supercapacitive performance of pristine $NaMPO_4$ (M = Mn, Co and Ni).

In this present work, we have demonstrated that the synthesis of sodium metal phosphates ($NaMPO_4$; M = Mn, Co and Ni) by solution combustion method using glycine-nitrate as precursors. The presence of nano-pores on the surface of the particles was clearly observed from field emission scanning electron microscope image (FE-SEM). The intercalation/de-intercalation properties of Na ion in maricite-type structured $NaMnPO_4$ were investigated. The orthorhombic maricite-type $NaNiPO_4$ nanoparticles provided higher capacitance of 368 F g^{-1} compared to hexagonal high-temperature phase of $NaCoPO_4$ (249 F g^{-1}) and maricite-type of $NaMnPO_4$ (195 F g^{-1}) in 1 M NaOH electrolyte. A hybrid supercapacitor is fabricated using $NaNiPO_4$ and activated carbon (AC) as positive and negative electrodes, respectively. The hybrid supercapacitor delivered excellent electrochemical performances relative to the commercially available device (AC||AC).

2. Experimental section

2.1 Materials

Sodium nitrate ($NaNO_3$), manganese nitrate tetrahydrate ($Mn(NO_3)_2 \cdot 4H_2O$), cobalt nitrate hexahydrate ($Co(NO_3)_2 \cdot 6H_2O$), nickel nitrate hexahydrate ($Ni(NO_3)_2 \cdot 6H_2O$), ammonium dihydrogen phosphate ($NH_4H_2PO_4$), glycine ($C_2H_5NO_2$), sodium hydroxide (NaOH) and aqueous ammonia ($NH_3 \cdot H_2O$) were purchased from Merck and used as received without further purification.

2.2 Synthesis of $NaMPO_4$, (M = Mn, Co and Ni)

For the synthesis of maricite-type $NaMnPO_4$, a stoichiometric amount of $Mn(NO_3)_2 \cdot 4H_2O$ (2.073 g), $NaNO_3$ (0.8499 g) and $NH_4H_2PO_4$ (1.150 g) were dissolved in desired amount of distilled water and mixed with the above solutions. The desired amount of glycine was dissolved in distilled water and poured into above solution. In this reaction, oxidant to fuel ratio was maintained as 1. Further, the pH of the precursor solution was adjusted to 7 by adding ammonia solution. The resulting solution was placed on hot plate at 200 °C for dehydration. After complete dehydration, the remaining solid mass was transferred into muffle furnace and the temperature was raised to 300 °C. After 10 minutes, decomposition occurred with gradual release of gaseous by-products. The final foamy product was collected after grinding it on agate mortar pestle and then used for further characterization. The foamy product was calcined at 400 °C for 3 h to form the single phase $NaMnPO_4$. The similar procedure was repeated for the synthesis of $NaCoPO_4$ and $NaNiPO_4$ by using $Co(NO_3)_2 \cdot 6H_2O$ and $Ni(NO_3)_2 \cdot 6H_2O$, respectively, as cation precursors. Here, the single phase of $NaNiPO_4$ was obtained after 700 °C calcinations and $NaCoPO_4$ phase was obtained without any calcinations.

2.3 Characterization techniques

Phase formation was identified by powder X-ray diffractometer (Bruker, D8 advance) with CuKα radiation. A quantitative two-phase full-profile Rietveld refinement was performed by using WinCSD program package. To investigate the morphology of the prepared samples, JEOL JEM 2100 High Resolution Transmission Electron Microscope (HRTEM) with 200 kV acceleration voltages was used. The surface area and pore size distribution of the composites were investigated by N_2 adsorption–desorption experiments at 77 K using Micromeritics ASAP 2010 surface area analyser. The electrochemical performances of $NaMPO_4$, (M = Mn, Co and Ni) were investigated using cyclic voltammetry (CV) and galvanostatic charge–discharge techniques. The electrochemical experiments were carried out in three electrode system using platinum wire as a counter electrode. Ag/AgCl and Hg/HgO were used as a reference electrode. Aqueous solution of 1 M Na_2SO_4, 1 M NaCl, 1 M $NaNO_3$ and 1 M NaOH were used as electrolyte. The cyclic voltammetry and galvanostatic charge–discharge studies of the composites were carried out using SP-150, Bio-Logic Science Instruments in room temperature.

2.4 Electrode preparation

To prepare active electrode material, $NaMPO_4$ (80 wt%), carbon black (15 wt%) and polyvinlidene fluoride (PVDF) (5 wt%) were suspended in 0.4 mL of *N*-methyl-2-pyrrolidinone (NMP) to form a slurry. The slurry was coated on a small piece of graphite sheet (area of coating, 1 cm^2). The loaded active material was approximately 2 mg in each case. Activated carbon (AC) was purchased from Aldrich with surface area of ~1800 m^2 g^{-1}. To prepare active negative electrode material, AC (90 wt%) and polyvinlidene fluoride (PVDF) (10 wt%) were used. A hybrid full cell (AC||$NaNiPO_4$) was fabricated by employing a polypropylene separator.

3. Results and discussion

3.1 Structural analysis

XRD patterns of combustion synthesized sodium metal phosphates ($NaMPO_4$, M = Mn, Co and Ni) are shown in Fig. 1(a–c).

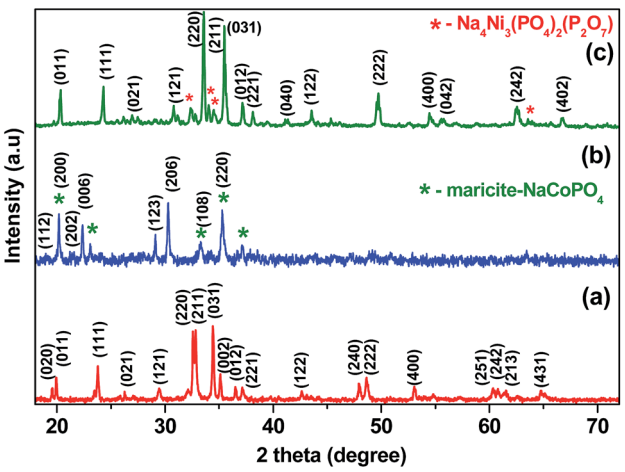

Fig. 1 XRD patterns of combustion synthesized (a) $NaMnPO_4$, (b) $NaCoPO_4$ and (c) $NaNiPO_4$.

Table 1 Lattice parameters of the $NaMPO_4$ (M = Mn and Co) phases in comparison with the literature data

Composition	Space group	*a*, Å	*b*, Å	*c*, Å	*V*, Å^3	Reference
$NaMnPO_4$	*Pmnb*	6.9053(9)	9.085(2)	5.1149(7)	320.9(2)	This work
$NaMnPO_4$	*Pmnb*	6.9041(1)	9.0882(1)	5.1134(1)	320.8	22
$NaCoPO_4$	$P6_5$	10.169(3)	—	23.868(7)	2137.5(9)	This work
h-$NaCoPO_4$	$P6_5$	10.166(1)	—	23.881(5)		JCPDS no. 52-335

The observed diffraction maxima for $NaMnPO_4$ (Fig. 1(a)) are basically matched with the standard diffraction pattern of maricite-type phase (JCPDS no. 84-0852). Full profile Rietveld refinement confirms the phase composition of $NaMnPO_4$ (see Fig. S1†) and allows establishing the lattice parameters of the orthorhombic $NaMnPO_4$. Refined values of the cell dimensions of $NaMnPO_4$ in comparison with the literature data for the reference compound are given in Table 1. The calculated lattice parameters are consistent with the reported values.

On the other hand, the majority of observed diffraction peaks of combustion synthesized $NaCoPO_4$ (Fig. 1(b)) are matched with the standard diffraction pattern of the high temperature β-phase of $NaCoPO_4$ (JCPDS no. 52-0335), which belongs to the family of stuffed tridymites. As it is derived from the quantitative XRD phase analysis, performed by two-phase Rietveld refinement, the sample shows coexistence of two $NaCoPO_4$ polymorphs – 77 wt% of hexagonal $NaCoPO_4$ phase and 23 wt% of orthorhombic maricite-type $NaCoPO_4$ phase (Fig. S2†). Lattice parameters of combustion synthesized $NaCoPO_4$ is well matched with reported high temperature hexagonal $NaCoPO_4$ (Table 1).

From the XRD pattern of $NaNiPO_4$ (Fig. 1(c)), orthorhombic maricite-type $NaNiPO_4$ is detected as the main phase. Besides $NaNiPO_4$, this sample contains $Na_4Ni_3(PO_4)_2(P_2O_7)$. According to the two-phase Rietveld refinement, the weight ratio of $NaNiPO_4$ and $Na_4Ni_3(PO_4)_2(P_2O_7)$ phases in the sample is 81 : 19 (Fig. 2). At the Rietveld refinement procedure, the atomic positions in the $NaMnPO_4$ structure[22] are taken as a starting model for the refinement of $NaNiPO_4$ structural parameters. For the secondary $Na_4Ni_3(PO_4)_2(P_2O_7)$ phase the atomic coordinates from ref. 23 are taken; these values are fixed during the refinement procedure.

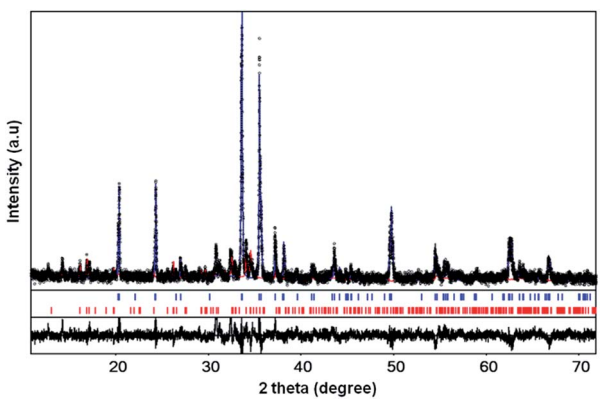

Fig. 2 Graphical results of the Rietveld refinement of the $NaNiPO_4$ sample showing presence of $NaNiPO_4$ (81 wt%, blue) and $Na_4Ni_3(PO_4)_2(P_2O_7)$ (19 wt%, red) phases.

Structural parameters of the $NaNiPO_4$ compound, obtained for the first time in the present work, are in excellent agreement with the literature data for the isotypical $NaMPO_4$ (M = Co, Fe, Mn) compounds. In particular, the lattice parameters in the $NaMPO_4$ series (Table 2) increases systematically with increasing ionic radii of M^{2+} ions and the unit cell volumes increase almost linearly in accordance with Vegard's law (Fig. 3).[3] The values of refined lattice parameters, positional and displacement parameters of atoms in $NaNiPO_4$ structure are presented in Table 3. Bond length and bond angles in the $NaNiPO_4$ structure calculated from the refined structural parameters are tabulated in Table S1.† According to our knowledge, no lattice parameters or atomic coordinates in the $NaNiPO_4$ structure are reported in the literature so far.

Similar to the related $NaMPO_4$ maricite-type compounds with Mn, Fe and Co,[22,24,25] the $NaNiPO_4$ structure can be described as edge-sharing chains of distorted NiO_6 octahedra running parallel to the [100]-direction (Fig. 4). Neighbouring chains are cross-connected by almost regular PO_4 tetrahedra, thus form large cavities in which the Na ions are located. The bond length and bond angles inside PO_4 tetrahedra in $NaNiPO_4$ structure (Table S1†) are similar to those in the related $NaMPO_4$ compounds,[22,24,25] and the average bond length of 1.537 Å corresponds well to the length of P–O bonds in phosphates. The NiO_6 octahedra are rather distorted, with two compressed and two stretched bonds (Table S1†). Besides, distortion of NiO_6 octahedra is manifested itself in a significant deviation of the intra-octahedral O–Ni–O bond angles from 90° (Table S1†). Like as in the related $NaMPO_4$ compounds, coordination polyhedra of Na ions could be also considered as octahedral, however the distortion of NaO_6 polyhedra is much more pronounced in comparison with NiO_6 octahedra (Table S1†).

3.2 Morphological analysis

In general, the morphological features are important to mend the electrochemical performance of the material. The formation of porous particles is the characteristic features of combustion method and the amount of pores mainly depend upon the amount of gases released during the reaction. Fig. 5(a) shows the SEM image of $NaMnPO_4$. It can be seen that the particles are having micrometer in size. The measured sizes of the particles are to be 0.02 to 0.6 μm using scion image software. TEM image (inset of Fig. 5(a)) of $NaMnPO_4$ further supports the formation

Table 2 Lattice parameters of $NaNiPO_4$ sample in comparison with the literature data for the related maricite-type $NaMPO_4$ (M = Co, Fe, Mn) compounds

Composition	Space group	*a*, Å	*b*, Å	*c*, Å	*V*, Å^3	Reference
$NaNiPO_4$	*Pmnb*	6.7373(7)	8.7735(10)	5.0336(6)	297.5(1)	This work
$NaCoPO_4$	*Pnma*	8.871(3)	6.780(3)	5.023(1)	302.1	JCPDS no. 87-1016
	Pnma	8.896(1)	6.8007(9)	5.0341(7)	304.5	JCPDS no. 88-481
$NaFePO_4$	*Pmnb*	6.867	8.989	5.049	311.6	JCPDS no. 29-1216
	Pnma	8.990	6.862	5.047	311.3	JCPDS no. 89-816
$NaMnPO_4$	*Pmnb*	6.9041(1)	9.0882(1)	5.1134(1)	320.8	JCPDS no.84-852

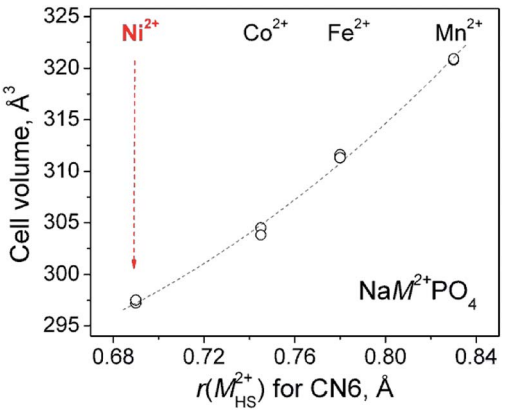

Fig. 3 Dependence of the unit cell volumes in $NaMPO_4$ (M = Ni, Co, Fe, Mn) series on the ionic radii of M^{2+} cations.

Table 3 Crystallographic data for $NaNiPO_4$ structure (space group *Pmnb*, *Z* = 4, *a* = 6.7373(7) Å, *b* = 8.7735(10) Å, *c* = 5.0336(6) Å)

Atoms, sites	*x*/*a*	*y*/*b*	*z*/*c*	$B_{iso/eq}$, Å^2
Na, 4*c*	3/4	0.8544(15)	0.553(2)	1.5(3)
Ni, 4*a*	0	0	0	1.1(2)
P, 4*c*	1/4	0.8206(11)	0.535(2)	1.1(3)
O1, 4*c*	1/4	0.882(2)	0.243(2)	0.5(4)
O2, 8*d*	0.4365(14)	0.8756(15)	0.6732(15)	0.7(4)
O3, 4*c*	1/4	0.6442(14)	0.539(3)	0.3(5)

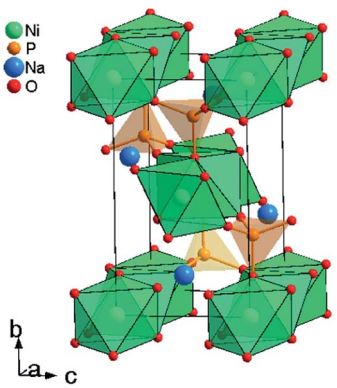

Fig. 4 $NaNiPO_4$ structure as a frame of the columns of edge-shared NiO_6 octahedra connected *via* PO_4 tetrahedra.

of larger size particles. Here, the agglomeration of the particles may be due to the high temperature calcination. Similarly, the spherical like particles are observed in $NaCoPO_4$ (Fig. 5(b)) and $NaNiPO_4$ (Fig. 5(c)). Subsequently, the presence of porous on the surface of the particles is clearly visible. On the other hand, in $NaNiPO_4$, the presence of smaller sized particles also observed compared to $NaCoPO_4$. Hence, the formation of microsized particles are due to the aggregation of smaller sized particles. So, the presence of pores and smaller sized particles may facilitate to improve the charge storage by the reduction of diffusive path lengths and improves the electrode/electrolyte contact area.[30,31]

3.3 Surface area analysis

The N_2 adsorption–desorption isotherms and pore size distribution (BJH-plot) of nanoporous $NaMPO_4$ (M = Mn, Co and Ni) particles are shown in Fig. 6. The observed type IV isotherm and BJH-plot for the $NaNiPO_4$ and $NaCoPO_4$ particles indicates the presence of mesopores on the surface of the particles. For $NaMnPO_4$, type II isotherm was observed, which confirms the nonporous nature of the particles. Hence, all these well substantiates the FE-SEM result. The calculated specific surface area (S_{BET}) of $NaMnPO_4$, $NaCoPO_4$ and $NaNiPO_4$ porous particles are 17.7, 22.6 and 18.7 m^2 g^{-1} respectively. The pore size distributions of the samples are calculated by using Barrett–Joyner–Halenda (BJH) method. The obtained average pore diameter of the $NaCoPO_4$ (~4 nm) and $NaNiPO_4$ (~4 nm) particles indicates the presence of mesopores. The high surface area and mesoporous structure of $NaCoPO_4$ and $NaNiPO_4$ nanoparticles when compared with $NaMnPO_4$ will provide more active reaction sites and improve the ions transport.[30]

3.4 Electrochemical analysis

In order to well understand the working potential window, redox potential of the active species and charge storage kinetics of the electrode, the cyclic voltammogram analysis was carried in different aqueous electrolytes. CV curves of $NaMnPO_4$ in different electrolytes including 1 M Na_2SO_4, 1 M NaCl, 1 M $NaNO_3$ and 1 M NaOH are given in Fig. 7. Overall, the potential dependent and independent current regions are observed based on the electrolytes. Specifically, the potential independent current response or rectangular shape CV curves was observed in 1 M NaCl electrolyte. It infers that the contribution of charge storage was mainly due to the EDLC type *i.e.*, adsorption–desorption of ions at the electrode/electrolyte interfaces. On the

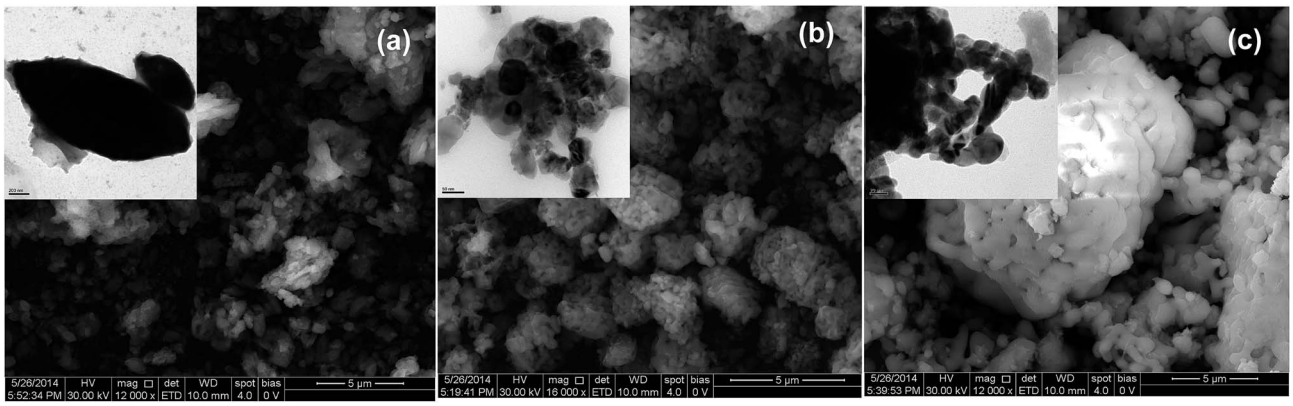

Fig. 5 FE-SEM images of nanoporous (a) $NaMnPO_4$, (b) $NaCoPO_4$ and (c) $NaNiPO_4$ particles (inset) TEM image.

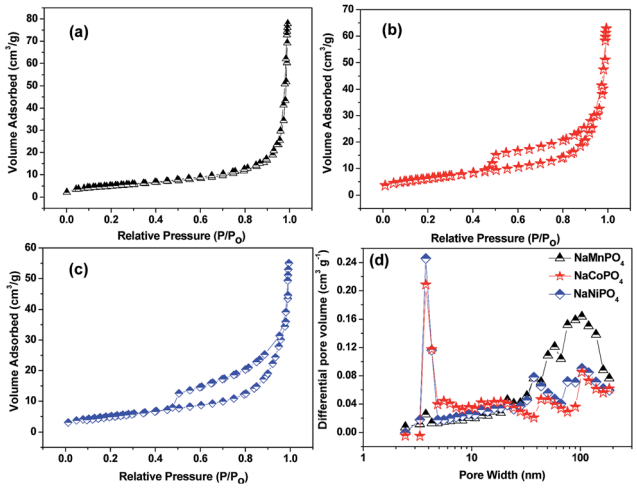

Fig. 6 (a) N_2 adsorption–desorption isotherms of (a) $NaMnPO_4$, (b) $NaCoPO_4$ and (c) $NaNiPO_4$. (d) Pore-size distributions of $NaMPO_4$.

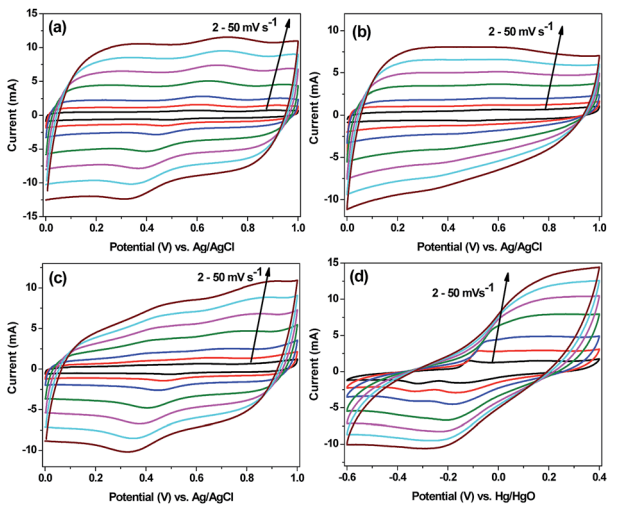

Fig. 7 CV curves of $NaMnPO_4$ in (a) 1 M Na_2SO_4, (b) 1 M NaCl, (c) 1 M $NaNO_3$ and (d) 1 M NaOH at various scan rates of 2, 5, 10, 20, 30, 40 and 50 mV s^{-1}.

other hand, a small redox peak (a potential independent current region) was observed for $NaMnPO_4$ at 0.59 V and 0.62 V *vs.* Ag/AgCl in 1 M Na_2SO_4 and 1 M $NaNO_3$ electrolytes, respectively, that revealed the occurrence of intercalation/de-intercalation of Na^+ ions. Similar type of redox peaks have been reported for MnO_2,[26a,b] NH_4MnPO_4,[26c] and Na_xMnO_2.[26d] The possible charge storage mechanism of $NaMnPO_4$ in 1 M Na_2SO_4 and 1 M $NaNO_3$ electrolyte is as follows[26]

$$Na_{1-x}MnPO_4 + xNa^+ + xe^- \leftrightarrow NaMnPO_4 \quad (1)$$

where, x is the mole fraction of inserted sodium ions. The potential difference between the anodic and cathodic peak is smaller than 56 mV, which indicates the good reversibility of the electrode. However the major contribution of the charge storage in neutral aqueous electrolyte depends on adsorption–desorption of Na^+ ions.

Interestingly, a well-defined oxidation/reduction peaks were obtained in 1 M NaOH electrolyte (Fig. 7(d)), which indicates the pseudocapacitive behavior of $NaMnPO_4$ electrodes. The observed redox peaks in the potential +0.015/−0.281 V *vs.* Hg/HgO is due to the Faradic redox reaction of Mn as explained from the Pour-baix diagram.[27] The calculated specific capacitances[30a] are 219, 132, 123 and 113 F g^{-1} for 1 M NaOH, 1 M NaCl, 1 M Na_2SO_4 and 1 M $NaNO_3$ respectively, at 2 mV s^{-1}. The difference in specific capacitance of $NaMnPO_4$ at different electrolytes is due to the difference charge storage mechanism. This may be explained based on the pH and ionic solvation radius of the electrolytes. According to the Pour-baix diagram of Mn, the Mn^{2+} ions involve in redox reactions only in alkali aqueous (1 M NaOH) electrolytes and not in neutral aqueous electrolytes like NaCl, $NaNO_3$ and Na_2SO_4. The observed redox peaks of $NaMnPO_4$ in NaOH electrolyte is mainly due to the electron transfer between Mn^{3+} and Mn^{2+} ions.

Similarly, the ionic solvation radius of OH^- (3.00 Å) ions is low compared to NO_3^- (3.35 Å), Cl^- (3.32 Å) and SO_4^- (3.79 Å) ions. Therefore the electrolyte OH^- ions can easily diffuse into the pores of the electrode that lodges more number of ions which in turn high specific capacitance.[28,29] In other words, the ions with smaller ionic solvation radius having high ionic conductivity in aqueous solutions that improves the maximum

number of ions to interact with active electrode. Subsequently it creates more active sites in the electrode material.[30b] Overall, low ionic solvation radius of electrolyte anions and pH of the electrolyte has favourably improved the electrochemical performances.

Fig. 8(a) shows the comparative CV curve of $NaMPO_4$ at 10 mV s^{-1} and Fig. 8(b and c) shows the CV curves of $NaNiPO_4$ and $NaCoPO_4$ in NaOH electrolyte at various scan rates. Similar to $NaMnPO_4$, both the materials also exhibited EDLC and intercalation/de-intercalation behavior in 1 M Na_2SO_4, 1 M NaCl, 1 M $NaNO_3$ and 1 M NaOH electrolytes. A couple of redox peaks were observed for both $NaNiPO_4$ and $NaCoPO_4$ nanoparticles in 1 M NaOH electrolyte due to intercalation/de-intercalation process, which is clearly seen in Fig. 8(a–c). The redox peak observed in $NaNiPO_4$ is due to the diffusion controlled reversible redox reaction of Ni(II) ↔ Ni(III).[31–33] The redox reaction of Co(II) ↔ Co(III) is the reason for the peaks obtained at 0.22/0.15 V *vs.* Hg/HgO in $NaCoPO_4$.[31,34] An extra pair of redox peak was observed at 0.55/0.45 V for $NaCoPO_4$ which is attributed to the redox reaction of Co(III) ↔ Co(IV).[34] The reproducibility of the redox peaks in the CV curves at higher scan rates confirms the good electronic and ionic transport of the material.[31,33] The capacitance calculated for $NaMPO_4$, in various scan rates of 2–20 mV s^{-1} is presented in Fig. 8(d). The capacitance is decreased with increase in scan rate which is due to the decrease in charge diffusion of electrolyte ions into the inner active sites at higher scan rates.[35] It is well agreed with morphological and surface area analysis results. However, the charge storage mechanism is vital role for storing energy.

For comparison, the calculated voltammetric specific capacitance of $NaMPO_4$ in all Na based aqueous electrolytes is presented in Fig. 9. It can be seen that the $NaMPO_4$ provides high capacitance in 1 M NaOH electrolyte than other electrolytes, due to its pseudocapacitive behaviour. Hence, it can be optimized that 1 M NaOH is the best electrolyte due to its smaller solvation sphere radius (OH^-), high ionic conductivity, and better reversibility of the electrode. Particularly, the

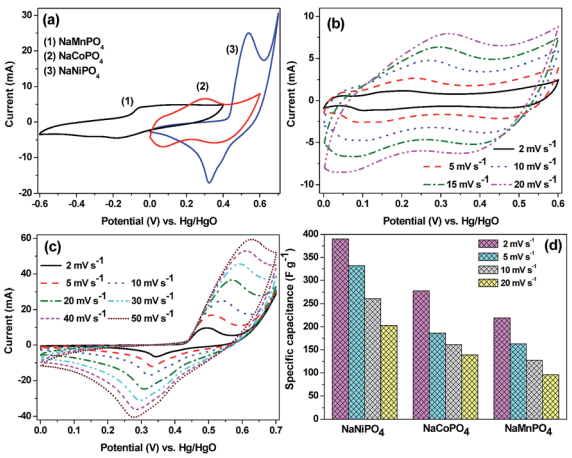

Fig. 8 CV curves of (a) $NaMPO_4$ at 10 mV s^{-1}, (b) $NaCoPO_4$ and (c) $NaNiPO_4$ in 1 M NaOH at different scan rates, (d) SC *vs.* scan rate for $NaMPO_4$ (M = Mn, Co and Ni).

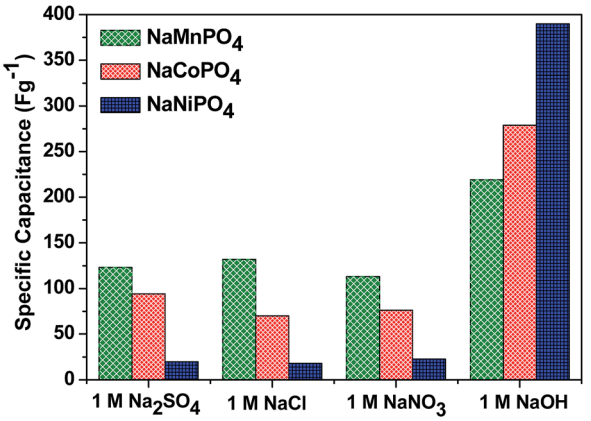

Fig. 9 Capacitance of $NaMPO_4$ (M = Mn, Co and Ni) in various electrolytes at 2 mV s^{-1} scan rate.

$NaNiPO_4$ deliver a high capacitance of 390 F g^{-1} at a scan rate of 2 mV s^{-1} compared to $NaMnPO_4$ (219 F g^{-1}) and $NaCoPO_4$ (279 F g^{-1}) due to the battery like behaviour and reversible redox reaction of Ni(II) ↔ Ni(III).[31–33] Among the studied sodium metal phosphates, $NaNiPO_4$ is electrochemically more active than $NaMnPO_4$ and $NaCoPO_4$. Based on the CV analysis, it is identified that the combination of $NaNiPO_4$ and 1 M NaOH are the best electrode and electrolyte. It is well known that the total amount of charge stored in the electrode is mainly due to the contribution of both capacitive and intercalation process.[26] However, the capacitive process consists of two mechanisms including surface redox pseudocapacitive and ions adsorption–desorption reaction at the electrode/electrolyte interface. According to Power's law, the scan rate dependence of CV current can be expressed as[36a–c]

$$i(V) = av^b \quad (2)$$

where, v is scan rate (V s^{-1}), a and b are the adjustable parameters. The slope of log i *vs.* log v at a fixed potential (V) gives the value of b. The value of b has two conditions like $b = 0.5$ for intercalation of ions into the electrode and $b = 1$ for capacitive process. It is the best way to know the charge storage kinetics at each potential. Fig. S3(a)† infers that the value of b is different in different potentials for $NaNiPO_4$. It shows that the value of b is closer to 0.5 at each potential in 1 M NaOH electrolyte. Hence, the CV curve is directly proportional to the square root of scan rate. It reveals that the $NaNiPO_4$ stores the charge based on intercalation/deintercalation mechanism rather than capacitive mechanism (Fig. S3(a)†). However, it reveals that the intercalation/deintercalation mechanism is dominant in 1 M NaOH electrolyte for $NaNiPO_4$. It is well substantiates the previous result.

The specific capacitance contribution from inner and outer surface of the electrode is calculated using Trasatti plot.[36a–d] The plot between specific capacitance and inverse square root of scan rate implies the specific capacitance contribution from outer surface of the electrode (Fig. S3(b)†). Similarly, the plot between specific capacitance *vs.* square root of scan rate implies

the specific capacitance contribution from the entire electrode (426 F g^{-1}) (Fig. S3(c)†). From this, it can be calculated that the specific capacitance contribution from inner surface of the electrode that is the difference between total surface of the electrode and outer surface of the electrode. Then, the calculated specific capacitance contribution from inner and outer surface of the electrode is 333 and 93 F g^{-1}. It witnessed that the electrode stores more charges in the inner surface of the electrode due to the low ionic solvation radius and high ionic mobility.

Hence, galvanostatic charge–discharge measurements were performed in 1 M NaOH for the $NaMPO_4$ electrodes and are given in Fig. 10. Two different discharge behaviours *i.e.*, linear and non-linear regions are observed for all the cases. The linear region implies that the electrode stores the charge based on adsorption–desorption reaction at the electrode surface. Similarly, the non-linear region is the evidence that the electrode stores the charge based on redox or intercalation mechanism. The asymmetric charge–discharge profiles were obtained for $NaMPO_4$ (M = Mn, Co and Ni) at all the current densities. It demonstrates the pseudocapacitive nature of the materials. The charge–discharge plateau regions were observed for $NaNiPO_4$ which demonstrates the battery type charge storage of the material. The plateau regions provide high specific capacitance (above 500 F g^{-1}) in narrow potential window and it shows high charge storage capability of the material. The calculated specific capacitance[33] at a current density of 2 mA cm^{-2} for $NaMnPO_4$, $NaCoPO_4$ and $NaNiPO_4$ is 163 F g^{-1}, 249 F g^{-1} and 368 F g^{-1}, respectively. The high capacitance of the $NaNiPO_4$ compared to other electrodes substantiates the CV results. The specific capacitance of $NaMPO_4$ as a function of current density is shown in Fig. 10(d). The specific capacitance was decreased with increase in current density which is normal behaviour. More than 64% of capacitance at low current density (2 mA cm^{-2}) was retained at higher current rates (10 mA cm^{-2}) for $NaCoPO_4$ and $NaNiPO_4$ which show high rate capability of the materials.

For practical applications, the cycle life of electrode material is an important parameter. The cycling stability of the materials was tested up to 1000 cycles at a current density of 10 mA cm^{-2}. The specific capacitance of $NaMPO_4$ as a function of cycle number is shown in Fig. 11. No significant capacitance fading was observed for $NaMnPO_4$ and $NaCoPO_4$ up to 1000 cycles. 93 and 96% of initial capacitance was observed for $NaMnPO_4$ and $NaCoPO_4$, respectively. In case of $NaNiPO_4$ more than 88% of initial capacitance was retained after 1000 cycles. The results showed good cycling stability of the materials in 1 M NaOH.

3.5 Asymmetric AC||$NaNiPO_4$ supercapacitor characteristics

From the above charge–discharge studies, $NaNiPO_4$ electrodes delivered more capacitance (368 F g^{-1}) compared to $NaMnPO_4$ and $NaCoPO_4$. Therefore an asymmetric full cell (AC||$NaNiPO_4$) was fabricated using $NaNiPO_4$ and activated carbon (AC) as positive and negative electrodes, respectively. The CV curve of $NaNiPO_4$ and AC in a three electrode system as recorded at a scan rate of 5 mV s^{-1} is shown in Fig. 12. The observed rectangular type CV curve of AC confirms the adsorption–desorption of electrolyte cations (Na^+) and EDLC behavior. The far negative working potential (−1.0 V) of the AC in aqueous electrolyte is promising to use this material as negative electrode

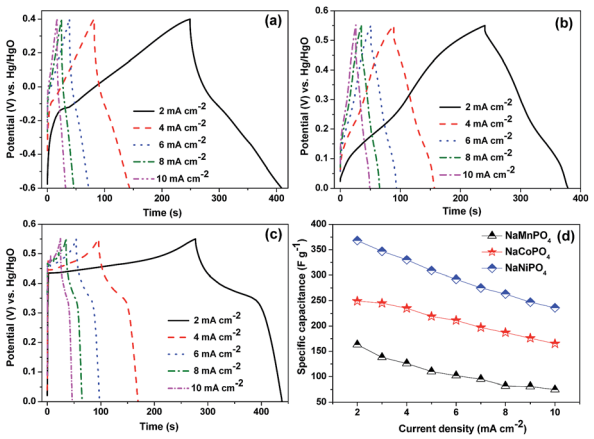

Fig. 10 Galvanostatic charge–discharge curves of (a) $NaMnPO_4$, (b) $NaCoPO_4$ and (c) $NaNiPO_4$ in 1 M NaOH electrolyte. (d) Specific capacitance *vs.* current density of $NaMPO_4$ (M = Mn, Co and Ni).

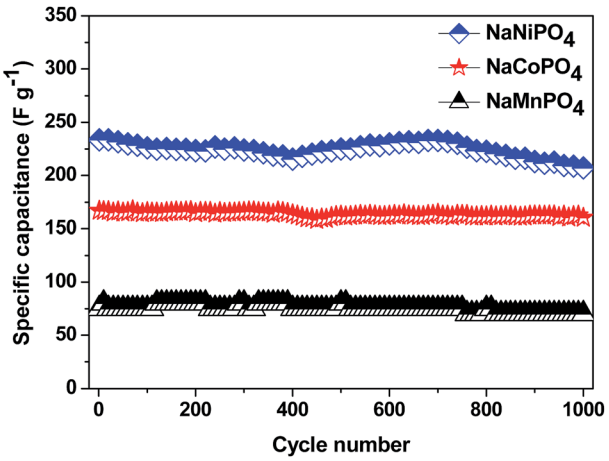

Fig. 11 Variation of the SC with cycle number at 10 mA cm^{-2} for $NaMPO_4$ (M = Mn, Co and Ni).

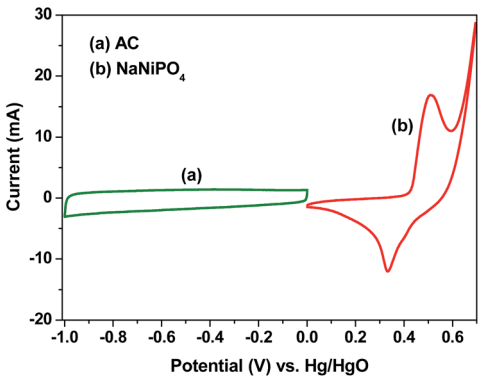

Fig. 12 CV curve of (a) AC and (b) $NaNiPO_4$ nanoparticles at a scan rate of 5 mV s^{-1}.

material for asymmetric supercapacitors. The specific capacitance calculated from the CV curve is 100 F g^{-1} for AC at a scan rate of 5 mV s^{-1}. In the same scan rate, $NaNiPO_4$ delivered a capacitance of 323 F g^{-1}. It is well known that the positive and negative charge should be balanced ($q_+ = q_-$) for fabrication of the full cell.[36e] The mass balancing will follow eqn (3),

$$\frac{m_+}{m_-} = \frac{c_-}{c_+} \times \frac{\Delta E_-}{\Delta E_+} \quad (3)$$

where, m is mass of the active material in the electrode and ΔE is the working potential of the material. On the basis of mass balancing, the calculated mass of negative electrode was 3.9 mg. So the mass loading of the negative electrode material was adjusted to 4 mg. The working potential of the cell is optimized from the CV curve (Fig. 12). The maximum working potential of the asymmetric cell is set to 1.6 V which is higher than that of the AC based symmetric supercapacitor (1.0 V) in alkali aqueous electrolyte.[37–39]

The CV measurements for the asymmetric full cell ($AC\|NaNiPO_4$) recorded at various scan rates is shown in Fig. 13(a). The redox peaks observed in the CV curves confirms the pseudocapacitance in positive electrode. An adsorption–desorption of electrolyte cations (Na^+) at the negative electrode (AC), with the formation of electrical double layer facilitate the charge storage process. The possible electrochemical charge storage reactions in the cell are, for the positive electrode is due diffusion controlled reversible redox reaction of Ni, and for the negative electrode,[40] the mechanism is given below

$$AC + xNa^+ + xe^- \leftrightarrow AC\,(xe^-)\|xNa^+ \quad (4)$$

(here, $\|$ indicates double layer).

Galvanostatic charge–discharge curves of the asymmetric capacitor were recorded at various current densities which are shown in Fig. 13(b). The mirror like form of charge discharge curve shows good electrochemical reversibility of the cell. Subsequently, the non-linear charge–discharge profile is observed which also well substantiates the CV results. The specific capacitance, energy density and power density of the full cell were calculated using the formulae reported else where.[30] The specific capacitance value obtained for the cell from the discharge curves is 56, 50, 41, 36 and 33 F g^{-1} at current densities 1, 2, 4, 6, 8 and 10 mA cm^{-2}, respectively. Fig. 13(c) compares the Ragone plots derived from charge–discharge curves at various current densities. The asymmetric capacitor delivers an energy density of 20 W h kg^{-1} at a power density of 138 W kg^{-1} and 12 W h kg^{-1} even at a high power density of 1358 W kg^{-1}. The power and energy density of the asymmetric $AC\|NaNiPO_4$ capacitor is comparatively higher than symmetric (AC||AC) and the current state-of-art electrical double layer capacitor (EDLC) technology.[41] Moreover, the energy density value of the capacitor is significantly higher than the reported $AC\|NaMnO_2$ (ref. 42) and $AC\|NaNi_{1/3}Co_{1/3}Mn_{1/3}PO_4$ (ref. 10) hybrid capacitors. However, the energy density is low compared with recent reports of $AC\|K_{0.27}MnO_2\cdot 0.6H_2O$ (ref. 43) and $AC\|Na_{0.35}MnO_2$ (ref. 44) supercapacitors. The cycle life of the cell was investigated up to 500 cycles. Fig. 13(d) shows the specific capacitance and coulombic efficiency of the cell tested for 500 charge–discharge cycles at a current density of 10 mA cm^{-2}. Superior coulombic efficiency (>95%) was observed for the asymmetric cell; capacitance is stable and above 70% of initial capacitance was retained up to 500 cycles. Overall, the maricite-type $NaNiPO_4$ is the promising electrode material for energy storage applications based on their good electrochemical reversibility, a high specific capacitance, a smaller particle size, a high surface area, mesoporous structure and a good cycle life.

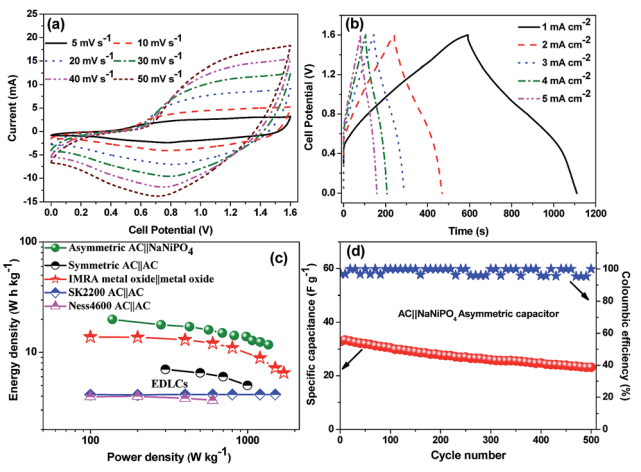

Fig. 13 (a) CV and (b) charge–discharge curves for $AC\|NaNiPO_4$ asymmetric supercapacitor, (c) Ragone plot, (d) cycling stability and coulombic efficiency of $AC\|NaNiPO_4$ asymmetric capacitor at 10 mA cm^{-2}.

4. Conclusions

In summary, $NaMnPO_4$ microstructures and $NaMPO_4$ (M = Co and Ni) nanoparticles were successfully synthesized by solution combustion synthesis technique. The formation of crystalline $NaMPO_4$ was identified by XRD Rietveld refinement. Structural parameters of new maricite-type $NaNiPO_4$ phase were refined. From N_2 absorption–desorption measurements specific surface area and pore size distributions of the samples were calculated. The electrochemical performance of the materials was first investigated in various Na based aqueous electrolytes and the charge storage mechanism was proposed. The $NaNiPO_4$ delivered a maximum capacitance of 368 F g^{-1} due to intercalation/de-intercalation like behaviour in 1 M NaOH electrolyte, nano meter size of the particles and reversible redox reaction of Ni. An asymmetric full cell ($AC\|NaNiPO_4$) was fabricated and it delivered a high specific capacitance (56 F g^{-1}) and energy density (20 W h kg^{-1}).

Acknowledgements

The authors would like to thank UGC-SAP, Government of India for the financial support. Also, one of the authors (BS) would like to thank DST-PURSE programme, Government of India for providing financial support to carry out this work successfully.

Notes and references

1 B. Dunn, H. Kamath and J. M. Tarascon, *Science*, 2011, **334**, 928.

2 M. S. Whittingham, *Science*, 1976, **192**, 1126.

3 (*a*) H. Pan, Y.-S. Hu and L. Chen, *Energy Environ. Sci.*, 2013, **6**, 2338; (*b*) J. Molenda, A. Kulka, A. Milewska, W. Zajac and K. Swierczek, *Materials*, 2013, **6**, 1656–1987.

4 (*a*) F. Wang, S. Xiao, Y. Hou, C. Hu, L. Liu and Y. Wu, *RSC Adv.*, 2013, **3**, 13059–13084; (*b*) F. Shi, L. Li, X.-L. Wang, C.-D. Gu and J.-P. Tu, *RSC Adv.*, 2014, **4**, 41910–41921; (*c*) S. P. Ong, V. L. Chevrier, G. Hautier, A. Jain, C. Moore, S. Kim, X. Ma and G. Ceder, *Energy Environ. Sci.*, 2011, **4**, 3680.

5 P. Moreau, B. Guyomard, J. Gaubicher and F. Boucher, *Chem. Mater.*, 2010, **22**, 4126–4128.

6 A. D. Tevar and J. F. Waitacre, *J. Electrochem. Soc.*, 2010, **157**, A870–A875.

7 J. P. Parant, R. Olazcuaga, M. Devalette, C. Fouassier and P. Hagenmuller, *J. Solid State Chem.*, 1971, **3**, 1–11.

8 J. Zhao, J. He, X. Ding, J. Zhou, Y. Ma, S. Wu and R. Huang, *J. Power Sources*, 2010, **195**, 6854–6859.

9 S. Komaba, C. Takei, T. Nakayama, A. Ogata and N. Yabuuchi, *Electrochem. Commun.*, 2010, **12**, 355–358.

10 M. Minakshi, D. Meyrick and D. Appadoo, *Energy and Fuels*, 2013, **27**, 3516–3522.

11 D. Kim, E. Lee, M. Slater, W. Lu, S. Rood and C. S. Johnson, *Electrochem. Commun.*, 2012, **18**, 66–69.

12 M. Nose, H. Nakayama, K. Nobuhara, H. Yamaguchi, S. Nakanishi and H. Iba, *J. Power Sources*, 2013, **234**, 175–179.

13 F. Sauvage, L. Laffont, J. M. Tarascon and S. Skaarup, *Inorg. Chem.*, 2007, **46**, 3289–3294.

14 D. Yuan, W. He, F. Pei, F. Wu, Y. Wu, J. Qian, Y. Cao, X. Ai and H. Yang, *J. Mater. Chem. A*, 2013, **1**, 3895–3899.

15 M. Minakshi and D. Meyrick, *J. Alloys Compd.*, 2013, **555**, 10–15.

16 K. T. Lee, T. N. Ramesh, F. Nan, G. Botton and L. F. Nazar, *Chem. Mater.*, 2011, **23**, 3593–3600.

17 S.-M. Oh, S.-T. Myung, J. Hassoun, B. Scrosati and Y.-K. Sun, *Electrochem. Commun.*, 2012, **22**, 149–152.

18 A. K. Padhi, K. S. Nanjundaswamy and J. B. Goodenough, *J. Electrochem. Soc.*, 1997, **144**, 1188–1194.

19 H. Pan, Y.-S. Hu and L. Chen, *Energy Environ. Sci.*, 2013, **6**, 2338–2360.

20 Y. Zhu, Y. Xu, C. Luo and C. Wang, *Nanoscale*, 2013, **5**, 780–787.

21 K. Zhagib, J. Trottier, P. Hovington, F. Brochu, A. Guerfi, A. Mauger and C. M. Julien, *J. Power Sources*, 2011, **196**, 9612–9617.

22 J. Moring and E. Kostiner, *J. Solid State Chem.*, 1986, **61**, 379–383.

23 P. G. Nagornyi, A. A. Kapshuk, A. N. Sobolev and N. V. Golego, *Kristallografiya*, 1996, **41**, 835–838.

24 J. N. Bridson, S. E. Quinlan and P. R. Tremaine, *Chem. Mater.*, 1998, **10**, 763–768.

25 R. Hammond and J. Barbier, *Acta Crystallogr., Sect. B: Struct. Sci.*, 1996, **52**, 440–449.

26 (*a*) S. Pang and A. M. Anderson, *J. Mater. Chem.*, 2000, **15**, 2096–2106; (*b*) Y.-H. Chu, C.-C. Hu and K.-H. Chang, *Electrochim. Acta*, 2012, **61**, 124–131; (*c*) H. Pang, Z. Yan, W. Wang, Y. Wei, X. Li, J. Li, J. Chen, J. Zhang and H. Zheng, *Int. J. Electrochem. Sci.*, 2012, **7**, 12340–12353; (*d*) L. Mai, H. Li, Y. Zhao, L. Xu, X. Xu, Y. Luo, Z. Zhang, W. Ke, C. Niu and Q. Zhang, *Sci. Rep.*, 2013, **3**(1718), 1–6.

27 M. Pourbaix, *Atlas of Electrochemical Equilibria in Aqueous Solutions*, Pergamon, New York, 1966.

28 C.-C. Hu and C.-C. Wang, *J. Power Sources*, 2004, **125**, 299–308.

29 F. Cheng, C. Hc, D. Shi, H. Chen, J. Zhang, S. Tang and D. E. Finlow, *Mater. Chem. Phys.*, 2011, **131**, 268–273.

30 (*a*) B. Senthilkumar, M. Danielle, Y.-S. Lee and R. Kalai Selvan, *RSC Adv.*, 2013, **3**, 16542–16548; (*b*) K. V. Sankar, D. Kalpana and R. K. Selvan, *J. Appl. Electrochem.*, 2012, **42**, 463–470.

31 B. Senthilkumar, K. Vijaya Sankar, R. Kalai Selvan, M. Danielle and M. Manickam, *RSC Adv.*, 2013, **3**, 352–357.

32 C. C. Hu, J. C. Chen and K. H. Chang, *J. Power Sources*, 2013, **221**, 128–133.

33 G. Wang, L. Zhang, J. Kim and J. Zhang, *J. Power Sources*, 2012, **217**, 554–561.

34 M.-C. Liu, L.-B. Kong, X.-J. Ma, C. Lu, X.-M. Li, Y.-C. LuO and L. Kang, *New J. Chem.*, 2012, **36**, 1713–1716.

35 M. Aghazadeh, A. N. Golikand and M. Ghaemi, *Int. J. Hydrogen Energy*, 2011, **36**, 8674–8679.

36 (*a*) M. Sathiya, A. S. Prakash, K. Ramesha, J. M. Tarascon and A. K. Shukla, *J. Am. Chem. Soc.*, 2011, **133**, 16291–16299; (*b*) J. Duay, S. A. Sherrill, Z. Gui, E. Gillette and S. Bok Lee, *ACS Nano*, 2013, **7**, 1200–1214; (*c*) H. Yina, C. Song, Y. Wang, S. Li, M. Zeng, Z. Zhang, Z. Zhu and Ke. Yu, *Electrochim. Acta*, 2013, **111**, 762–770; (*d*) K. V. Sankar and R. K. Selvan, *RSC Adv.*, 2014, **4**, 17555–17566; (*e*) J. Cao, Y. Wang, Y. Zhou, J.-H. Ouyang, D. Jia and L. Guo, *J. Electroanal. Chem.*, 2013, **689**, 201–206.

37 E. G. Calvo, F. Lufrano, P. Staiti, A. Brigandi, A. Arenillas and J. A. Menendez, *J. Power Sources*, 2013, **241**, 776–782.

38 X. Sun, X. Zhang, H. Zhang, D. Zhang and Y. Ma, *J. Solid State Electrochem.*, 2012, **16**, 2597–2603.

39 L.-B. Kong, M. Lu, J.-W. Lang, Y.-C. Luo and L. Kang, *J. Electrochem. Soc.*, 2009, **156**, A1000–A1004.

40 Y. Zhao, Q. Y. Lai, Y. J. Hao and X. Y. Ji, *J. Alloys Compd.*, 2009, **471**, 466–469.

41 A. F. Burke, *Proc. IEEE Veh. Power Propulsion Conf. (VPPC''05)*, 2005, pp. 356–366.

42 Q. T. Qu, Y. Shi, S. Tian, Y. H. Chen, Y. P. Wu and R. Holze, *J. Power Sources*, 2009, **194**, 1222–1225.

43 Q. Qu, L. Li, S. Tian, W. Guo, Y. P. Wu and R. Holze, *J. Power Sources*, 2009, **195**, 2789–2794.

44 B. H. Zhang, Y. Liu, Z. Chang, Y. Q. Yang, Z. B. Wen, Y. P. Wu and R. Holze, *J. Power Sources*, 2014, **253**, 98–103.

